

# MONITORING OF AERODYNAMIC PRESSURES FOR VENUS EXPRESS IN THE UPPER ATMOSPHERE DURING DRAG EXPERIMENTS BASED ON TELEMETRY

Sylvain Damiani<sup>(1,2)</sup>, Mathias Lauer<sup>(1)</sup>, and Michael Müller<sup>(1)</sup>

<sup>(1)</sup> ESA/ESOC; Robert-Bosch-Str. 5, 64293 Darmstadt, Germany; +49 6151900;  
[first.last@esa.int](mailto:first.last@esa.int)

<sup>(2)</sup> GMV GmbH; Robert-Bosch-Str. 7, 64293 Darmstadt, Germany; +49 61513972970;  
[sylvain.damiani@gmv.com](mailto:sylvain.damiani@gmv.com)

**Abstract:** *The European Space Agency Venus Express spacecraft has to date successfully completed nine Aerodynamic Drag Experiment Campaigns designed in order to probe the planet's upper atmosphere over the North pole. The daily monitoring of the campaign is based on housekeeping telemetry. It consists of reducing the spacecraft dynamics in order to obtain a timely evolution of the aerodynamic torque over a pericenter passage, from which estimations of the accommodation coefficient, the dynamic pressure and the atmospheric density can be extracted. The observed surprising density fluctuations on short timescales justify the use of a conservative method to decide on the continuation of the experiments.*

**Keywords:** *Venus Express, Drag Experiments, Attitude Dynamics, Aerodynamic Torque.*

## 1. Introduction

The European Space Agency's Venus Express spacecraft has been orbiting around Venus since 2006, and its mission has now been extended until 2014. During the extended mission, it has already successfully accomplished 9 Aerodynamic Drag Experiment campaigns until September 2012. Each campaign aims at probing the planet's atmospheric density at high altitude and next to the North pole by lowering the orbit pericenter (down to 165 km of altitude), and observing its perturbations on both the orbit and the attitude of the probe. An overview of the operational process as well as first results have already been published (see [1] and [5]). While [5] uses tracking data to determine density estimates from the relative deceleration of the spacecraft as it crosses the atmosphere, [1] obtains the same information from the reaction wheels additional momentum load (the on-board accelerometers are not sensitive enough to be useful at those altitudes). Both rely on a model of the evolution of the atmospheric density with respect to the altitude. The purpose of this paper is to describe and discuss the method used to timely reduce the spacecraft's attitude dynamics over the crossing of the atmosphere, in order to extract the aerodynamic torque. The operationally relevant characterization of the atmosphere, namely the dynamic pressure, as well as a characteristic of the surface interactions between the spacecraft and the atmosphere, the accommodation coefficient, are further obtained by comparing the measurements to predictions based on an enhanced spacecraft geometric model. While more sensitive to data noise and to attitude disturbances, this method can be applied even when the spacecraft is not in inertial attitude, and allows a sampling of the dynamic pressure variation over the few minutes of atmospheric crossing.

We first describe in detail the method used to obtain a timely evolution of the aerodynamic

torque. We then explain the model and software implemented in order to model this environmental torque and give the principles to estimate two parameters, including the atmospheric density. Finally, we stress the difficulties encountered when trying to build an atmospheric model reliable enough for the design of the experiments to come.

## 2. Reduction of the aerodynamic torque

### 2.1. Operational setup

Venus Express describes a polar elliptical orbit of approximately 24h around Venus, with a pericenter above the North pole. As described in [1], the drag experiments are implemented during seasonal periods when the Sun is in the orbit plane. Then the pericenter altitude temporary stops decaying because of the Sun's 3<sup>rd</sup> body effect, and the ground track is close to the terminator. This allows for a small variation of the local time over the pericenter (several degrees) and a better stability of the encountered maximum atmospheric density from one day to the other. Considering that the atmosphere starts at 180 km of altitude, a crossing takes about 200 s during which high rate telemetry is enabled. Torque experiments are implemented over some of the pericenters, with an immobile spacecraft in inertial frame and solar panel orientations tuned in order to enhance external aerodynamic torques. The other pericenters remain dedicated to normal science operations, including slews and solar panel maintained perpendicular to the Sun direction with occasional repositioning. During torque experiment dedicated orbits, 30 minutes of high rate telemetry are available around the pericenter time. For the other orbits such that the altitude goes below 180 km, 6 minutes of data are also recorded. These data are down-linked a few hours later at the beginning of the first contact with the ground, in order to check that the spacecraft is not endangered by the atmosphere, namely that the maximum load on each reaction wheel is below 4 mNm and the estimated heat flux below 18 W/m<sup>2</sup>. If the first constraint is likely to be violated for the next experiment, the solar panel angles are modified. As for the second constraint, its violation leads to the commanding of an escape maneuver to increase the pericenter altitude, therefore terminating the campaign.

### 2.2. Data reduction principle

As mentioned above, the principle of the extraction of the aerodynamic torque is to remove from the attitude controller demanded torque all the known torques through an analysis of the spacecraft dynamics. Newton's laws of rotational motion applied to the spacecraft and expressed in its body fixed frame give at a given instant:

$$\sum \vec{T}_{\text{ext}} = \vec{T}_g + \vec{T}_s + \vec{T}_d = \dot{\vec{H}} + \vec{\omega} \times \vec{H} \quad (1)$$

where  $\vec{T}_g$  is the gravity gradient torque,  $\vec{T}_s$  the solar radiation torque,  $\vec{T}_d$  the aerodynamic torque,  $\vec{H}$  the total spacecraft angular momentum (including the moving parts) and  $\vec{\omega}$  its angular rate. Therefore, Eq. 1 can be used to extract the aerodynamic torque once all the other terms have been computed. They are summarized in Tab. 1, and the inputs necessary to compute them in Tab. 2.

**Table 1. Torques governing the spacecraft dynamics**

Torque origin	Formula	Input timed data	Potential mismodelings and perturbations	Order of magnitude (mNm)	Comment
Gravity gradient	Eq. 2	Spacecraft orbital position, Venus orbital position, spacecraft attitude, solar panels position	Spacecraft mass repartition (fluids)	1	Order zero gravity model
Solar radiation pressure	see section 3.2	Spacecraft orbital position, Sun orbital position, spacecraft attitude, solar panels position	Optical properties, spacecraft geometrical model	0,1	Eclipses must be taken into account
Spacecraft rigid body dynamics	Eq. 3	Spacecraft angular rate and acceleration, solar panel angular position	Spacecraft mass repartition (fluids)	Experiments: 0.1 Slews: 40	Includes the reaction wheels in the inertia
Reaction wheels generated torque	Eq. 5	Wheels required torque in spacecraft frame	Axes misalignments, friction instabilities	Experiments: 5 Slews: 40 Max: 50	Compensates the rest
Reaction wheels gyroscopic contribution	Eq. 4	Spacecraft angular rate, wheel angular momentum	Axes misalignments	Slews: 5	
Solar panels	N/A	Spacecraft angular rate, solar panels angular position, rate and acceleration	Flexible modes (theoretically over 0.4 Hz)	50	Not enough telemetry for reduction, so not modeled.
Fluids	N/A	N/A	N/A	neglected	Not modeled, but possible small effect in the total spacecraft inertia
Instrument scanner	N/A	N/A	N/A	Outside experiments: 1	Not modeled

**Table 2. Inputs necessary to reduce the aerodynamic torque.**

Input	In formulas	Source
Sun orbital position	$\vec{r}_S$ : JD2000 referential frame ( km )	DE405 ephemeris
Venus orbital position	$\vec{r}_V$ : JD2000 referential frame ( km )	DE405 ephemeris
Spacecraft orbital position	$\vec{r}$ : JD2000 referential frame ( km )	Orbit determination
Spacecraft attitude	$Q$ : attitude matrix from JD2000 to spacecraft frame	On-board estimated attitude quaternion, low rate telemetry (0.25 Hz)
Spacecraft angular rate	$\vec{\omega}$ : in spacecraft frame ( rad · s <sup>-1</sup> )	Gyroscopes, high rate telemetry (8 Hz)

Input	In formulas	Source
Spacecraft angular acceleration	$\dot{\vec{\omega}}$ : in spacecraft frame ( $rad \cdot s^{-2}$ )	Differentiation of the spacecraft angular rate
Solar panels angular position	$\alpha_i, i \in \{+, -\}$ : + (resp. -) for the panel on the spacecraft +Y (resp. -Y) side ( $rad$ )	Low rate telemetry (0.25 Hz)
Solar panels angular rate (for completeness)	$\dot{\alpha}_i, i \in \{+, -\}$ : + (resp. -) for the panel on the spacecraft +Y (resp. -Y) side ( $rad \cdot s^{-1}$ )	Differentiation of the solar panels angular position
Solar panels angular acceleration (for completeness)	$\ddot{\alpha}_i, i \in \{+, -\}$ : + (resp. -) for the panel on the spacecraft +Y (resp. -Y) side ( $rad \cdot s^{-2}$ )	Differentiation of the solar panels angular rate
Reaction wheels angular momentum	$\vec{H}_W$ : Vector of size 4 ( $N \cdot m \cdot s$ )	Filtered tachometer counters, high rate telemetry (8 Hz)
Wheels required torque in spacecraft frame	$\vec{T}_W$ : Vector of size 3 ( $N \cdot m$ )	High rate telemetry (8 Hz)

The gravity gradient torque is given by:

$$\vec{T}_g = 3\mu \|\vec{r} - \vec{r}_v\|^{-5} (Q \cdot (\vec{r} - \vec{r}_v) \times I \cdot (Q \cdot (\vec{r} - \vec{r}_v))) \quad (2)$$

where  $I$  is the spacecraft total inertia tensor expressed in spacecraft frame and  $\mu$  the gravitational constant of Venus.

Spacecraft rigid body dynamics:

$$\vec{T}_{SC} = I \cdot \dot{\vec{\omega}} + \vec{\omega} \times I \cdot \vec{\omega} \quad (3)$$

Reaction wheels gyroscopic contribution:

$$\vec{T}_{W,g} = \vec{\omega} \times A_{W,c}^t \cdot \vec{H}_W \quad (4)$$

where  $A_{W,c}$  is a 4x3 matrix, each row being the cosines of the ground calibrated rotation axis of one of the four wheels in spacecraft frame.

Reaction wheels generated torque:

$$\vec{T}_{W,a} = A_{W,c}^t \cdot A_{W,s} \cdot (A_{W,s}^t \cdot A_{W,s})^{-1} \cdot \vec{T}_W \quad (5)$$

where  $A_{W,s}$  is the on-board software wheels alignment matrix. It has not been updated on-board because the effects are noticeable only during slews, and in that case the attitude controller can cope with this uncertainty in the produced torque.

### 2.3. Challenges in the data reduction

The first difficulty comes from the noise of the received telemetry. As seen on Fig. 1, the reaction wheel commanded torque is low pass filtered by the on-board controller, and the reaction wheel angular momentum as well via a Kalman filter which also estimates the friction torque. However, the angular rates directly come from the gyroscopes and are dominated by high frequency noise. We have therefore applied low pass filters (moving averages) at all the steps of the data reduction involving telemetry.

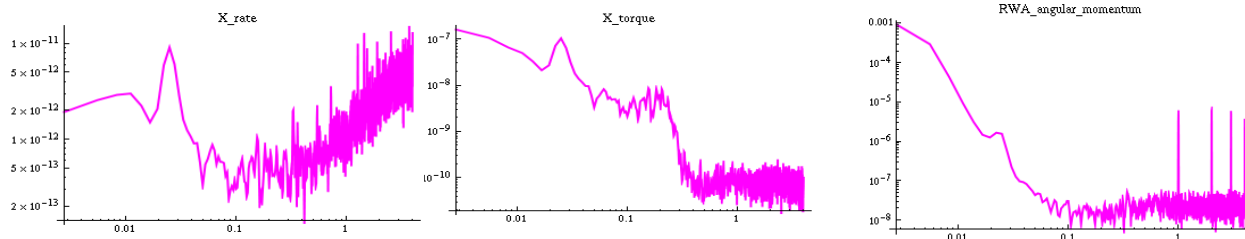


**Figure 1. Power spectral densities of the input high rate telemetry. Data obtained after an experiment. From left to right: rate around  $\vec{x}$ , reaction wheel demanded torque around  $\vec{x}$ , and angular momentum of the first wheel. Horizontal axis in Hz.**

Secondly, the commanded torques by the attitude controller to the reaction wheels is given in spacecraft frame before being dispatched among the 4 existing wheels using the knowledge of their axis direction. However, while trying to reduce the data during slews, we noticed some biases that could not be explained by the aerodynamic torques. The problem was solved by calibrating the wheels alignment matrix during slews far from the pericenter, with estimated misalignments of up to  $1^\circ$ . Despite this improvement, some biases are still observed when fast slews occur at pericenter, which could be related to errors in the inertia matrix or delays in the telemetry timing.

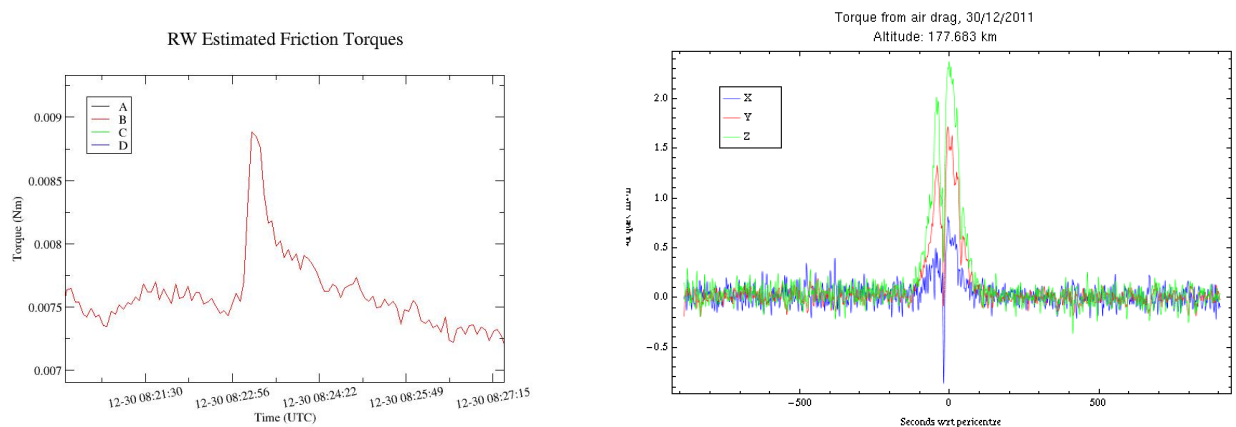


**Figure 2. Effect of a spike of the wheel friction torque on the data reduction.**

If the disturbances caused by ASPERA instrument's scanner have been avoided by a careful planning of its operations, other ones cannot be avoided by planning. For instance, Venus

Express' reaction wheels have been subject for years to friction torque instabilities which can occur at any time. Some of them take the form of spikes (sudden increase immediately followed by a return to the normal value) which are outside the bandwidth of the friction torque compensation control loop, therefore appear as external torques after the data reduction. Fig. 2 present a case when the spike occurred right at pericenter, where the signal to noise ratio is the best.

Finally, for completion it has been attempted to remove the perturbations brought by the solar panel repositioning. However, those are quick moves, therefore produce big torques (see Fig. 3), and unfortunately the frequency of the telemetry providing the angle evolution is too low for an accurate reduction.

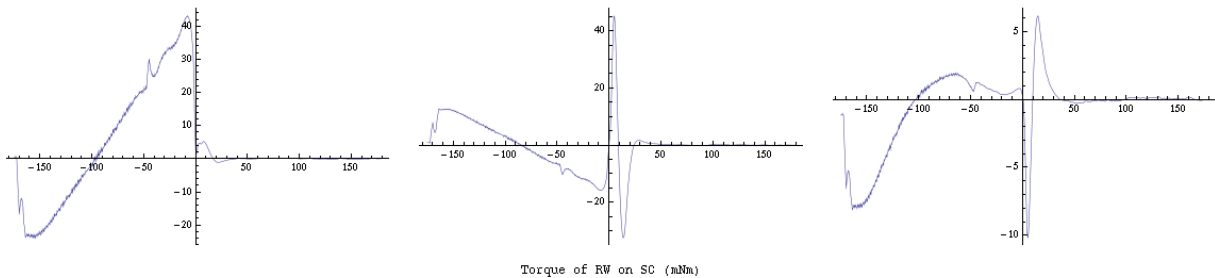


**Figure 3. Wheels commanded torque during a fast slew ( $0.25^\circ/s$ ) followed by a repositioning of the panels ( $8^\circ$  in 10s) right at pericenter. There is one plot per spacecraft axis. The horizontal axis is in seconds from pericenter time.**

#### 2.4. Aerodynamic torque profiles

When the data reduction is successful, that is no bias remains and no unmodeled disturbance occur, and the spacecraft geometry is favorable, a clear signature of the aerodynamic torque appears.

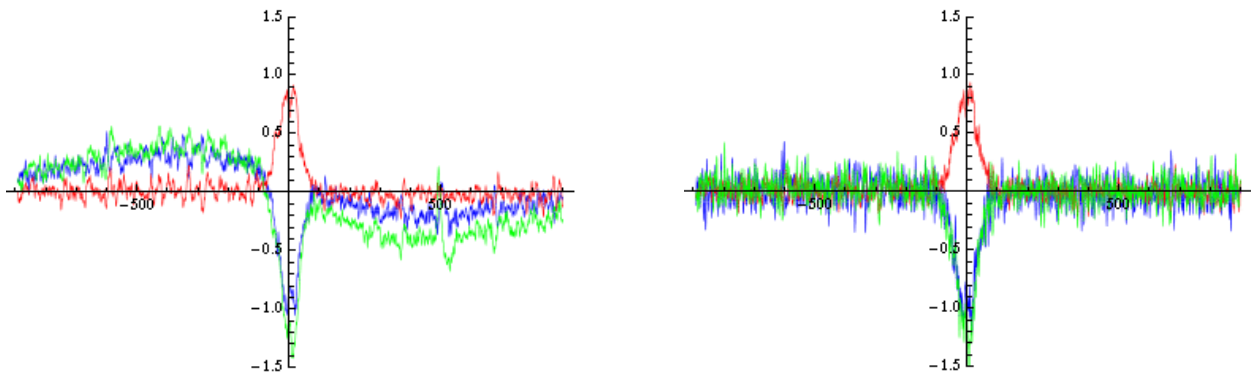


**Figure 4. Wheels commanded torque and reduced aerodynamic torque (in mNm) during a torque experiment for spacecraft X (blue), Y (red) and Z (green) axes.**

Figure 4 displays the attitude controller torque demand to the reaction wheels and the remaining external torque after reduction. The latter depicts a typical signal which emerges at low spacecraft altitude, peaks at the pericenter, reaching a signal to noise ratio of about 10 before

receding as the altitude increases again. This signal, which can without any doubt be attributed to the aerodynamic effects, is visible 200 s per pericenter passage. The attitude controller torque signal additionally contains a contribution from the gravity gradient, which is also symmetrical with respect to the pericenter, as well as a small spike at about 500 s due to a commanded attitude correction following the reentry of the star tracker into the attitude estimation loop. Until that moment, the star tracker was blinded by Venus and the attitude determination relied only on the propagation of the gyroscope provided angular rates.

Figure 5 provides an example of a successful reduction during a science pointing. In this case the wheel demanded torque is dominated by the following of the guidance attitude profile as well as the compensation of the gyroscopic torques, but after removal an aerodynamic torque contribution along spacecraft X and Y axes appears.

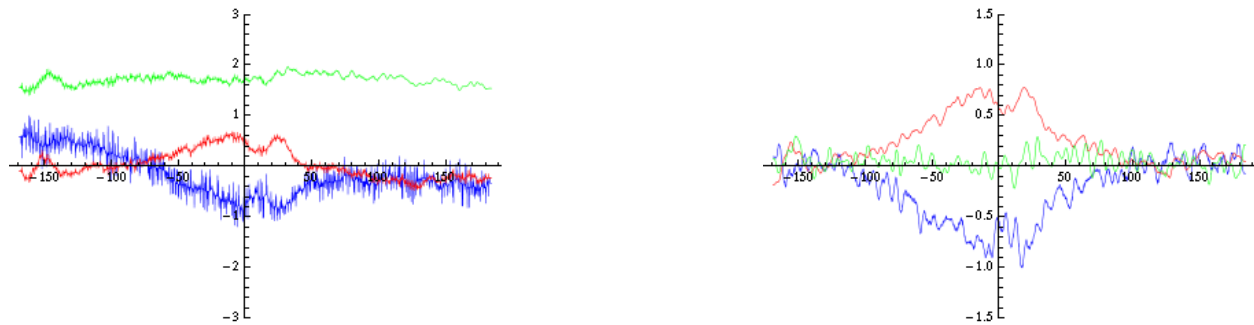


**Figure 5. Wheels commanded torque and reduced aerodynamic torque (in mNm) during normal science operations with a slow slew ( $0.1^\circ/\text{s}$ ).**

### 3. Aerodynamic torque modeling

#### 3.1. Method

The total aerodynamic torque results from the sum of all the momentum exchanges between the spacecraft surface and the encountered atmospheric particles. According to [5], in the case of Venus Express the particles are mainly atoms of oxygen, and the relevant regime is the hyper-thermal free-molecular flow. From [6], in a free-molecular flow, the incident flow is undisturbed by the presence of the body and the equilibrium velocity distribution of the incident molecules is changed only by collision with the body. This implies that momentum exchange due to molecules colliding with each other are neglected and only molecule-surface interactions are important. In addition, geometrically complicated surfaces can be easily treated by partitioning into simpler constituent surfaces except for complications due to shadowing and multiple surface collisions. In a hyper-thermal flow, the random thermal motion of the atmospheric molecules is neglected against the spacecraft velocity, which amounts to consider the incoming molecules as a collimated beam impinging on an element of surface area with a single characteristic velocity.

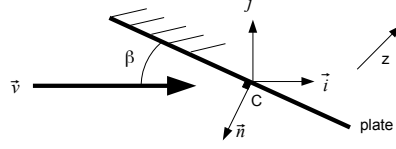


**Figure 6. Hyper-thermal free-molecular flow and flat plate. View in the plane containing the surface normal  $\vec{n}$  and the incident flow vector  $\vec{v}$ .  $C$  is the plate's centroid.**

Therefore, at a given instant, the aerodynamic torque can be expressed in spacecraft reference frame as

$$\vec{T}_d = \iint_S (\vec{r} - \vec{r}_G) \times \vec{F}(\vec{r}, \vec{v}) dS \quad (6)$$

where  $dS$  is a surface element at position  $\vec{r}$ ,  $\vec{r}_G$  is the center of mass position and  $\vec{v}$  is the incident molecular flow. Since the contribution of the movement of the spacecraft surface elements (slews and panel repositioning) can be neglected,  $\vec{v}$  is a constant in the integral.  $\vec{F}(\vec{r}, \vec{v})$  is the aerodynamic force. [6] gives a closed form of this force on a flat plate of area  $A$ , of outer normal vector  $\vec{n}$  such that  $\vec{n} \cdot \vec{v} < 0$  and a with centroid position  $\vec{r}_C$  (see also Fig. 6):

$$\vec{F}(\vec{r}_C, \vec{v}) = \frac{1}{2} \rho \|\vec{v}\|^2 A (C_D \vec{i} + C_L \vec{j}) \quad (7)$$

where  $\vec{i} = \frac{\vec{v}}{\|\vec{v}\|}$  and  $\vec{j} = \frac{(\vec{v} \times \vec{z}) \times \vec{v}}{\|(\vec{v} \times \vec{z}) \times \vec{v}\|}$ ,  $\vec{z}$  provides an absolute reference for the lift,  $\rho$  is the molecular flow density,  $C_D$  is the drag coefficient:

$$C_D = 2(\sigma_t + \sigma_n \frac{V_w}{\|\vec{v}\|} \sin \beta + (2 - \sigma_n - \sigma_t) \sin^2 \beta) \sin \beta \quad (8)$$

and  $C_L$  the lift coefficient:

$$C_L = (\sigma_n \frac{V_w}{\|\vec{v}\|} + (2 - \sigma_n - \sigma_t) \sin \beta) \sin 2\beta \quad (9)$$

In the latter two formulas,  $\beta = \arccos(-\vec{j} \cdot \vec{n})$  is the angle of attack,  $\sigma_n$  and  $\sigma_t$  are the momentum accommodation coefficients which relate the incident and reflected momentum fluxes.  $\sigma_n$  (resp.  $\sigma_t$ ) stands for the contribution normal (resp. tangential) to the surface. Those parameters do not have a simple physical formula, so they must be estimated. Similarly to [7], we have chosen to consider them equal and identical for all the spacecraft surfaces and all the conditions:

$$0 \leq \sigma_n = \sigma_t = \sigma \leq 1 \quad (10)$$

$V_w$  is the average velocity of the particles leaving the surface after full accommodation (that is, absorption and temperature equilibrium with the surface):

$$V_w = \sqrt{\frac{\Pi R T_w}{2\mu}} \quad (11)$$

where  $R$  is the universal gas constant,  $T_w$  the temperature of the accommodated and re-emitted molecules, assumed to be then at room temperature, and  $\mu$  atomic oxygen's molecular weight. In the case of Venus Express drag campaigns,  $V_w \approx 500 \text{ m s}^{-1} \ll \|\vec{v}\| \approx 10 \text{ km s}^{-1}$  so for simplicity we have discarded the terms in  $V_w$ . Consequently, Eq. 7 becomes:

$$\vec{F}(\vec{r}_C, \vec{v}) = -\frac{1}{2} \rho \|\vec{v}\|^2 A \left( \frac{\vec{v}}{\|\vec{v}\|} \cdot \vec{n} \right) 2 \left( \sigma \frac{\vec{v}}{\|\vec{v}\|} + 2(1-\sigma) \left( \frac{\vec{v}}{\|\vec{v}\|} \cdot \vec{n} \right) \vec{n} \right) \quad (12)$$

Assuming that the spacecraft has been decomposed into a set of  $N$  flat plates exposed to the flow, the total aerodynamic force around its center of mass can now be expressed as:

$$\vec{T}_d = -\frac{1}{2} \rho \|\vec{v}\|^2 \sum_k^N A_k \left( \frac{\vec{v}}{\|\vec{v}\|} \cdot \vec{n}_i \right) (\vec{r}_{C,k} - \vec{r}_G) \times 2 \left( \sigma \frac{\vec{v}}{\|\vec{v}\|} + 2(1-\sigma) \left( \frac{\vec{v}}{\|\vec{v}\|} \cdot \vec{n}_k \right) \vec{n}_k \right) \quad (13)$$

When the aerodynamic torque modeled in Eq. 13 is equaled to the measured one, one obtains 3 equations which allow in principle to resolve both the accommodation coefficient and the atmospheric density. Since we are assuming that the former is a constant for all the experiments, once it has been estimated (see section 3.5), the evolution of the density throughout an atmospheric crossing can be derived.

### 3.2. Software design

In Eq. 13, we have assumed that the spacecraft surface can be decomposed into a set of flat plates exposed to the incoming molecular flow, and that for each of them the normal vector, the area, and the center of pressure location are known.

This first statement requires that the spacecraft surface can actually be represented by a set of flat polygons. As depicted on Fig. 8, the gross shape of Venus Express consists of 4 main parts: the body (a box), two solar panels with hinges which can be rotated around the Y axis (flat plates), and the main high gain antenna dish. The latter has actually a circular shape and is protected by blanket of insulation material, which makes it look like a cone. However, by choosing a sufficient number of facets, it is also possible to represent it as a set of flat polygons.

To compute which area of a facet is exposed to the wind and the location of its effective center of pressure, the location of each of its vertices is first computed in the main spacecraft reference frame. Then, it is checked whether its normal vector has a negative projection against the incoming flow. If yes, the parts shaded by other faces are removed. Finally, the centroid location and the area of the remainder are determined (see section 3.3 for details on the used algorithms).

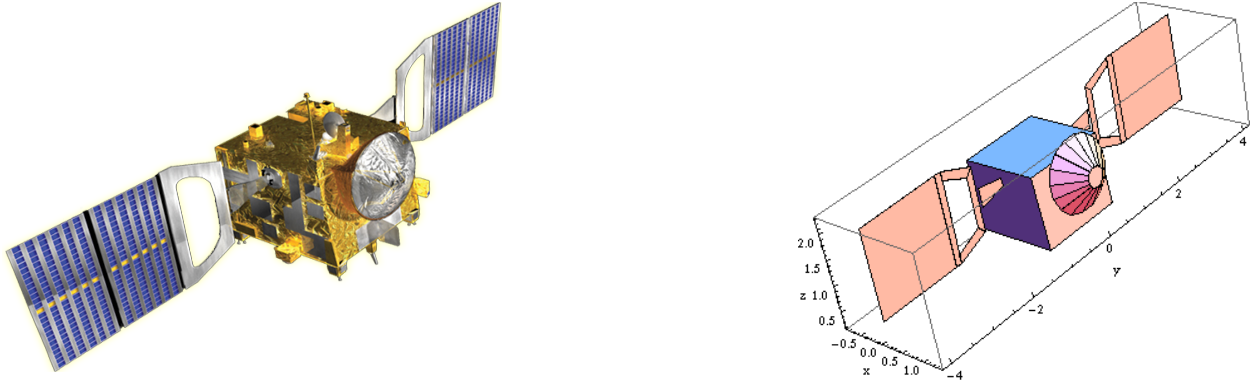


**Figure 7. Full spacecraft model (left) and used decomposition into flat polygons (right) with axes in meters.**

It is interesting to notice that this kind of problem is very similar the computation of the solar radiation pressure torque. Indeed, in both cases, the effect of the perturbation derives from an interaction between an incoming planar flow and the surface of the spacecraft. If secondary interactions are neglected, the only cross-coupling between two pieces of the surface is the mutual shading, and the total force and torque is the sum of the forces and torques on the pieces. Finally, in both cases, the force and torque of each piece  $k$  can be divided into a vector part  $\vec{f}$  weighted by a physical scalar term (a pressure  $P$ ) and a cross-section  $C_s$  :

$$\vec{T}_k = P C_s (\vec{r}_c - \vec{r}_g) \times \vec{f}(\vec{d}, \vec{n}_k, p_{k,1}, \dots, p_{k,l}) \text{ with } C_s = A \vec{d} \cdot \vec{n}_k \quad (14)$$

where  $\vec{d}$  is a normalized vector opposite to the incoming flow,  $\vec{n}_k$  the normal to the surface,  $A$  the area and the  $p_{\{k,1\}}, \dots, p_{\{k,l\}}$  are surface properties of piece  $k$ . Using this model, Tab. 3 summarizes the similarities between solar radiation and aerodynamic forces.

**Table 3. Correspondence aerodynamic - solar radiation effects**

	<b>Aerodynamic</b>	<b>Solar radiation</b>
Environment values	Spacecraft relative velocity with respect to the atmosphere $\vec{v}$ Atmospheric density $\rho$	Sun to spacecraft vector $\vec{s}$ Solar constant at 1 AU $K$
Anti flow direction $\vec{d}$	$-\frac{\vec{v}}{\ \vec{v}\ }$	$-\frac{\vec{s}}{\ \vec{s}\ }$
Pressure $P$	$\frac{1}{2} \rho \ \vec{v}\ ^2$	$\frac{K}{\ \vec{s}\ ^2} AU^2$
Surface properties	Accommodation coefficient $\sigma$	Absorption coefficient $\epsilon$ Ratio diffusive to total reflectivity $D$
Normalized force $\vec{f}$	$-2(\sigma \vec{d} + 2(1-\sigma)(\vec{d} \cdot \vec{n}) \vec{n})$	$-(\epsilon + (1-\epsilon)D) \vec{d} - (1-\epsilon)(2(1-D) \vec{n} \cdot \vec{d} + \frac{2}{3}D) \vec{n}$

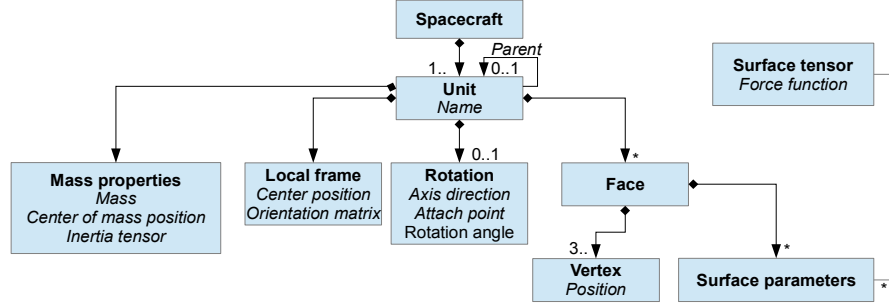


**Figure 8. UML like class diagram of the generic spacecraft model.**

Figure 8 provides a structure for all the information needed in order to compute a surface tensor. The units parental relationship builds a tree structure. The attach point, rotation axis direction and center of the local frame of an unit are expressed in parent's local frame (not relevant for the root of the tree), all the rest in unit's local frame. The outer normal to a face with index  $k$  is determined by its first 3 vertex positions  $\vec{x}_{k,i}, i=1...3$  :

$$\vec{n}_k = (\vec{x}_{k,2} - \vec{x}_{k,1}) \times (\vec{x}_{k,3} - \vec{x}_{k,1}) \quad (15)$$

The surface parameters number and semantic depend on the surface tensor model. The rotation angle of an unit is here the only time dependent variable. For simplicity the liquids are not included into the mass properties, but they are actually taken into account. Similarly, the dependency of the force applied on a face on the environmental conditions (flow direction and pressure) is not shown.

Table 3 and Fig. 8 illustrate how, for our purposes, we have been able to conveniently reuse a piece of software which has been used for years to provide to the orbit determination team an estimate of the acceleration generated by the solar radiation on the spacecraft.

### 3.3. Removing shaded parts of spacecraft faces

For a given spacecraft configuration (here the rotation angles of both solar panels), it is easy to compute the position of each face vertex in spacecraft reference frame. Once a given anti flow direction is known, one first filters out the non facing faces. Then one must determine which part of a remaining face is actually exposed to the flow by removing the shaded portions, which is a more computationally demanding problem commonly encountered in 3D computer graphics.

The first step always consists of expressing all the vertices in a frame the last unit vector of which is  $\vec{d}$ , such that the first 2 components give coordinates of the projected faces while the last one gives the precedence in terms of exposition to the flow (the altitude).

#### 3.3.1. Recursive grid

The first algorithm is the one which has been used for the solar radiation pressure acceleration on

ESA's interplanetary spacecraft [3]. It is similar to Warnock's algorithm [9], an efficient divide and conquer method to determine hidden surfaces. The principle is to partition the projected view of the spacecraft (as seen from the incoming flow), that is a set of overlapping polygons, into square pixels such that they intersect no polygon edge. Our FORTRAN implementation begins with an initial grid size, and can refine each grid element at most a given number of times. What's more, when a grid element has only 2 intersections with an edge, then it is accordingly split and the refinement stops. Figure 9 shows an example of a final grid after a few refinements, for which some parts of the spacecraft are missing while some pieces are added that should not be there. After the refinement phase, for each grid element centroid, it is checked into the projection of which polygons it is included, and the grid element is affected to the one with the highest altitude, resulting in an update of its visible cross section and centroid location.

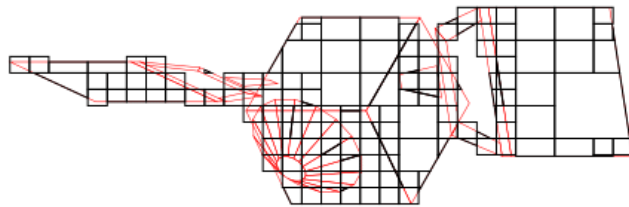


**Figure 9. Visualization of the projected faces (red polygons) and the pieces of the grid contributing to the force and torque (black polygons) for a low refinement level.**

The maximum error of this scheme can be controlled by the maximum number of iterative refinements. A trade-off must be found between this level and the computation time. For Venus Express, the initial grid size measures 1 m, and the smallest grid 4 mm (that is after 8 refinement steps).

### 3.3.2. Polygon boolean operations

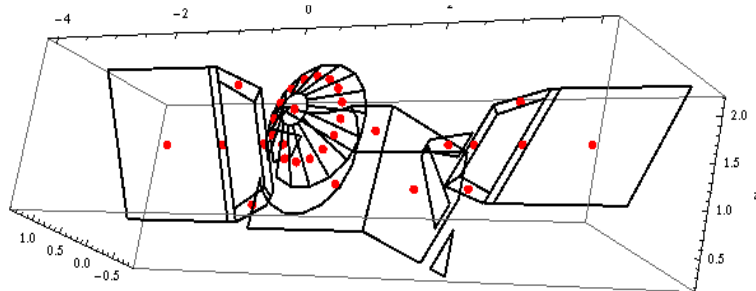


**Figure 10. Visualization of the kept spacecraft parts after removing the faces not facing the flow and clipping the remaining ones. The red dots are the final face centroid locations.**

The second algorithm was initially implemented in order to be able check the accuracy of the previous one. Indeed, it relies on boolean operations on the projected 3D polygons, but at the cost of a higher computation complexity. The principle is to compute the complete exact intersection of the set of polygons, in our case following the method proposed in [2]. After this decomposition, the same algorithm as in section 3.3.1 is applied, by replacing the grid elements by the intersection pieces. For clarity of inspection and speed up of that latter process, an union

of all the visible pieces of each polygon is incrementally computed. Figure 10 provides an example with the same incoming flow direction and spacecraft configuration as for Fig. 9. It reveals the parts of the spacecraft body which have been carved because of shading from a solar panel and the main high gain antenna.

Another advantage of this method is that it can handle any complex polygons, therefore is more robust to the structure of the geometrical model. To date, only a Mathematica prototype was developed, avoiding the need for an implementation of rational number operations which are not available in FORTRAN. Note however that it is also currently very slow: it takes a few minutes to obtain what the incremental grid method generates in one second.

### 3.4. Sensitivity to the parameters

In this section, we analyze the impact of the different parameters used to model the aerodynamic torque. The test cases are the actual conditions encountered by the probe as it crossed the atmosphere during the 9 first campaigns, that is a few minutes around pericenter for a total of 210 pericenters. Sometimes, a distinction is made between the pericenters dedicated to torque experiments, performed in inertial pointing with an immobile spacecraft, and the ones dedicated to normal science activities, which may contain slews and instrument scanner or solar panel repositioning. The inputs are basically the anti-flow direction, the solar panels orientation and the center of mass position. Unless specified, an accommodation coefficient of 0.89 was used. The outputs are the variations in spacecraft reference frame of the total torque around the center of mass. They are represented in polar coordinates, where the argument represents an angular difference (between 0 and 180°), and the radius a difference of norms in percent of the overall maximum torque. Negative angles actually indicate negative norm differences. No relative norm ratios were used because sometimes the reference torques can be close to null.

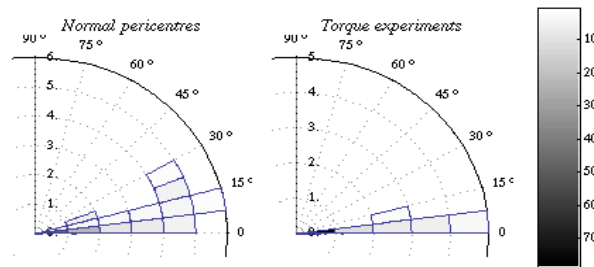


**Figure 11. Impact of the shading. Error in aerodynamic torque at pericenter when self shading is not taken into account, which means that some spacecraft parts can contribute although they should be discarded. The color code represents the cases counts.**

For example, the effect of the spacecraft self shading is represented on Fig. 11. It shows that the total torque norm is in general not much affected. As for the torque direction, the impact is also low during torque experiments, but a divergence of up to 30° can be reached during normal operations.

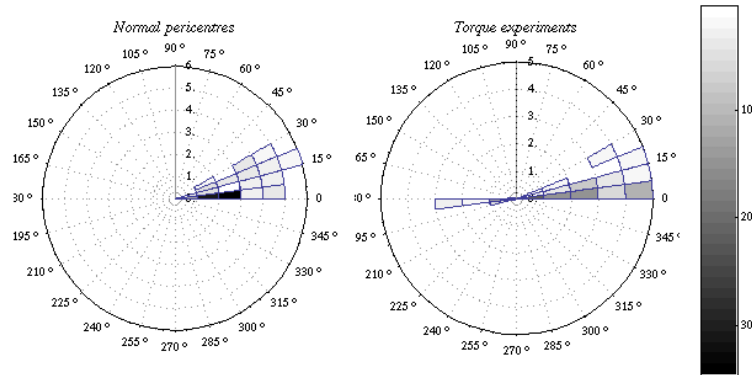


**Figure 12. Impact of the body and the antenna faces. Error in aerodynamic torque when spacecraft body and antenna are not included in the geometrical model. The color code represents the cases counts.**

On Fig. 12, the relative influence of the body and the main high antenna is summarized. During torque experiments, their influence cannot be neglected because they might change the torque direction by up to 30°.

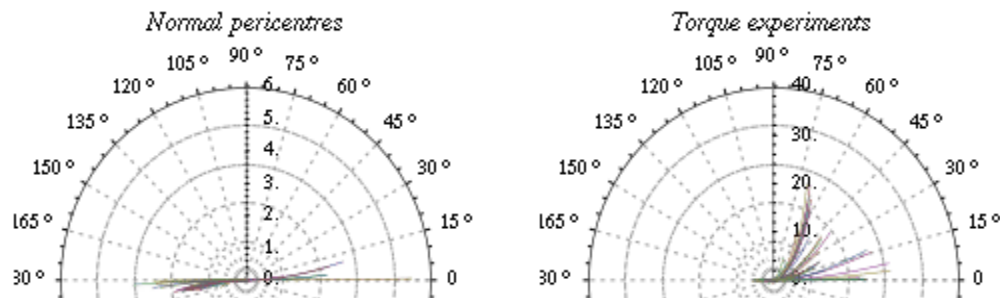


**Figure 13: Effect of the accommodation coefficient. Each line represents the evolution of the torque difference wrt. the torque obtained for with  $\sigma=1$  as  $\sigma$  varies from 1 to 0.8.**

On Fig. 13, the effect of the accommodation coefficient is analyzed for a plausible range  $0.8 \leq \sigma \leq 1$ . Since we have seen on Fig. 12 that the total torque depends mainly on the solar panels, and since it (as opposite to the aerodynamic force) is influenced by the differential orientation of the panels, it is clear that the accommodation coefficient has little impact during normal operations when the panels are parallel, whereas during torque experiments it can change significantly the result, especially during windmill experiments (see section 3.5).

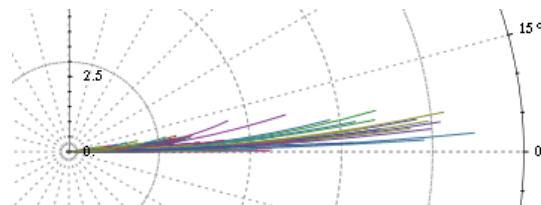


**Figure 14: Effect of the wind direction. Each line represents the torque evolution as the spacecraft crosses the atmosphere as compared to the torque at pericenter.**

As the spacecraft crosses the upper atmosphere, the relative wind direction can vary of up to  $35^\circ$  during normal operations, but remains within  $5^\circ$  of its direction at pericenter during torque experiments. Figure 14 shows that this evolution has an impact on the intensity of the aerodynamic torque, but not so much on its direction.

### 3.5. Design of the experiments

The experiments are meant to estimate the unknown parameters of Eq. 13, that is the density and the accommodation coefficient. The design method of the experiments is described in [1]. It focuses on the solar panel positions only since they provide the biggest contribution to the aerodynamic torque, and their position can be adjusted more freely than the attitude itself. There are two types of configurations, each one with a degree of freedom to tune the resulting torque in order to obtain the highest signal to noise ratio while staying within the allocated reaction wheel maximum torque of 4 mNm. To give an idea, we rewrite Eq. 7 with the following simplifications: the incoming flow vector is along  $-\vec{x}$  ( $\vec{i} = -\vec{x}$ ),  $\vec{z}$  is chosen as reference for the lift ( $\vec{j} = \vec{z}$ ), only the panels are considered, with area  $A = 3.8 m^2$ , angles of attack  $\beta_-$  (panel along -Y axis) and  $\beta_+$  (panel along +Y axis) and center of pressure positions with respect to the center of mass  $l\vec{z} \pm L\vec{y} \approx (0, \pm 2.9, 0.6) m$  :

$$\vec{T}_d = P A \begin{pmatrix} L(C_L(\beta_+) - C_L(\beta_-)) \\ -l(C_D(\beta_+) + C_D(\beta_-)) \\ L(C_D(\beta_+) - C_D(\beta_-)) \end{pmatrix} \quad (16)$$

In the first configuration, one panel (say -Y) is normal to the flow ( $\beta_- = 0$ ), and the contribution is provided by the second panel only. If we position the second panel parallel to the flow,  $\beta_+ = \pi/2$ , and the torque becomes:

$$\vec{T}_d = 2 P A (2 - \sigma) \begin{pmatrix} 0 \\ -l \\ L \end{pmatrix} \quad (17)$$

In this configuration, dynamic pressure and accommodation coefficient cannot be resolved independently. In the second configuration, called windmill,  $\beta_- = \pi - \beta_+$ . For instance if  $\beta_+ = \pi/4$  and  $\beta_- = 3\pi/4$ , the torque becomes:

$$\vec{T}_d = 2 P A \begin{pmatrix} L(\sigma + \sqrt{2}(1 - \sigma)) \\ -\sqrt{2}l(1 - \sigma) \\ 0 \end{pmatrix} \quad (18)$$

It is now possible to resolve first the accommodation coefficient from the ratios of the first two components of the torque, then the dynamic pressure from the norm ratios. In practice though, because of operational constraints, the flow direction cannot be always in the spacecraft (XZ) plane, therefore a windmill experiment is characterized by  $\beta'$  the projection of the angle of attack of the first panel into the (XZ) plane, and the angle between the flow direction and the Y

axis ( $\alpha'$ ,  $90^\circ$  ideally), which is the same for both panels. The accommodation coefficient is then obtained by maximizing the the scalar product between measured and modeled torque directions.

## 4. Results

### 4.1. Accommodation coefficient

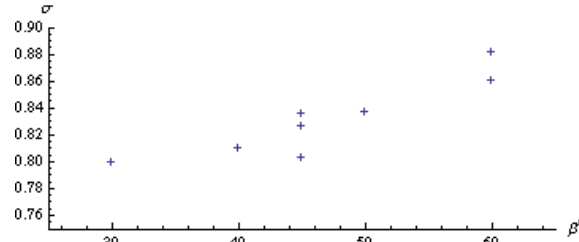


**Figure 15: Accommodation coefficient fitted during windmill experiments.  $\alpha' \approx 66^\circ$  for  $\beta' = 45^\circ$ , else  $\alpha' \approx 82^\circ$ .**

As mentioned in [7], the momentum accommodation coefficient is known to vary with the angle of attack. Figure 15 provides the estimates obtained after performing eight torque experiments in windmill configuration with different angles of attack. One can indeed observe a global monotonic increase of the accommodation with the angle of attack, however with significant uncertainty. For the computations of the dynamic pressure presented hereafter,  $\sigma = 0.89$  because this value was also employed as the energy accommodation coefficient, and as such it constitutes a worse case for the heat flux received by the probe.

### 4.2. Local dynamic pressure variations

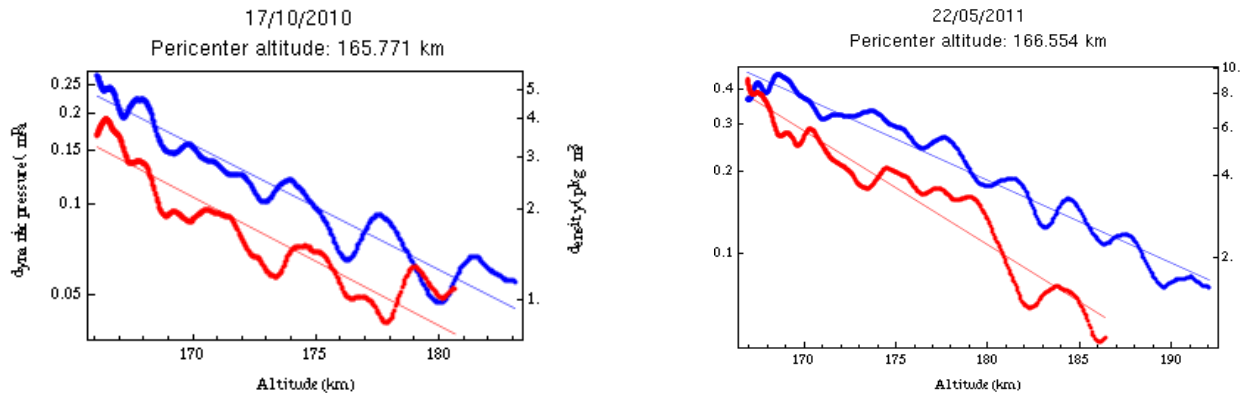


**Figure 16: Exponential decay with the altitude and impact of the local time for two passages, varying from  $83^\circ$  to  $90^\circ$  on the right and nearly constant on the left ( $88^\circ$  to  $88.2^\circ$ ). In blue (resp. red), data obtained before (resp. after) the pericenter. 10s of data have also been removed around the pericenter.**

In the sequel, we use indifferently density, the physical characteristic, and dynamic pressure, the operational relevant one, because the velocity variation is very small ( $9.8 \pm 0.02$  km/s) during a passage in the atmosphere. When observing the evolution of the dynamic pressure over one crossing, one clearly observes that it does not only depend on the altitude. On Fig. 16, the leftmost case gives the impression that a common scale height (density divided by  $e$  when the altitude increases by this length) of about 10 km can be extracted before and after the pericenter, whereas on the rightmost case the scale height is bigger over the more illuminated descending arc. Note that by local time, one means here the angle between spacecraft and Sun directions as seen from Venus. On Fig 17, the left case also enhances the asymmetries observed between descending and ascending arcs, with a maximum density shifted towards the more illuminated arc. The right case indicates that latitude and longitude of the sub-spacecraft point most probably also play a role.

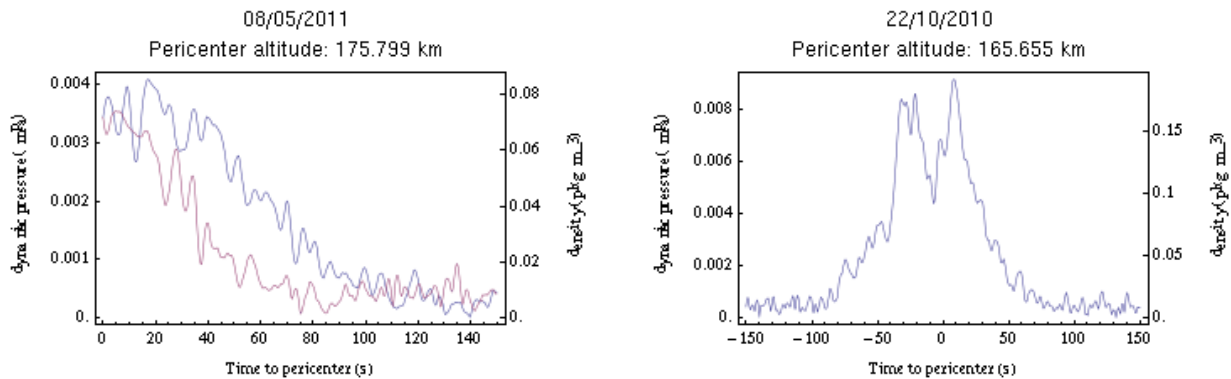


**Figure 17: To the left, asymmetry between before (blue, day side) and after (red, terminator) the pericenter. The local time increases linearly from  $75^\circ$  to  $90^\circ$ . To the right, local dynamic pressure peaks over one crossing.**

A significant variability (up to 100%) of the dynamic pressure at pericenter has also commonly been observed for measurements performed in successive orbits with yet very similar conditions. They might be related to variations in solar activity or to the atmospheric waves mentioned in [4].

### 4.3. Model for operations

Considering amount of parameters possibly involved to explain the variability of the atmospheric density, a trade-off had to be found within the operational resources in order to perform the experiments without endangering the spacecraft.

As mentioned in [1], the following simplifications have been made for the predictions from one torque experiment to the next (data reductions outside the actual experiments were not taken into account): one fixed accommodation coefficient (0.89), symmetrical density profile with respect to pericenter and fixed scale height of 5 km (maximum measured). What's more, the effort to update the solar panel angles was performed only when the predicted load on a wheel would violate the limit of 4 mNm, not when the predicted aerodynamic torque signal to noise ratio would be too low. Therefore, the low reference scale height led us to limit the sensitivity after

the first experiments of a campaign, while the spacecraft's pericenter altitude was still decreasing, sometimes resulting in very poor torque aerodynamic torque signatures.

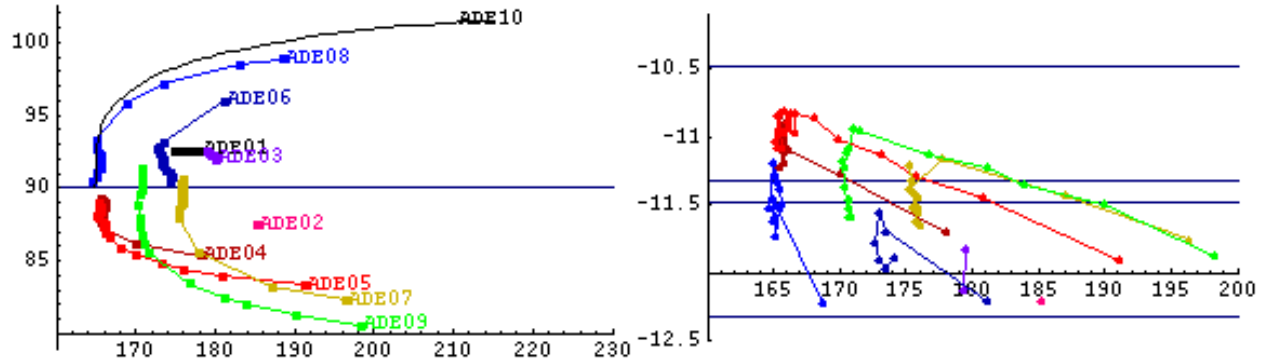


**Figure 18: Aerodynamic Drag Experiment campaigns summary. To the left, operational conditions in terms of pericenter altitude and local time. To the right, decimal logarithm of the measured density at pericenter as a function of the altitude. There is one color per campaign, and one point per torque experiment. ADE 10 is to occur in December 2012.**

The same assumptions were made in order to prepare the future campaigns, while additionally taking into account the local time at pericenter. Figure 10 summarizes the measurements performed over the first nine campaigns and provides a prediction for the tenth, still to come at the time of writing.

## 5. Conclusion

This paper has described in detail the method used to monitor the air drag campaigns for Venus Express. Although conservative, it has been able to produce clear aerodynamic torque signatures over the pericenter during torque experiments and favorable routine science operations. If aerobreaking activities [8] are confirmed, this method will also be applied to their monitoring.

## 6. References

- [1] Arona, L.; Müller, M.; Huguet, G.; Tanco, I.; Keil, N., "Venus Express Solar Arrays Rotation Experiments To Measure Atmospheric Density", Proceedings of the 22nd International Symposium on Spacecraft Flight Dynamics, 2011.
- [2] Brandt, J., 2D-Polygon-Clipping-Algorithmen für eingebettete Echtzeitsysteme, Arbeitsgruppe Reaktive Systeme, Fachbereich Informatik, Universität Kaiserslautern, 2003.
- [3] Fainberg, J. and Herfort, U.. "Solar Radiation Pressure Force and Torque", Technical report RO-ESC-TN-5529, European Space Agency, 2001.
- [4] Müller-Wodarg, I.C.F.; Forbes, J.M.; Keating, G.M. "The thermosphere of Venus and its exploration by a Venus Express Accelerometer Experiment". Planetary and Space Science, 54, 2006.

- [5] Rosenblatt, P.; Bruinsma, S. L.; Müller-Wodarg, I. C. F.; Häusler, B.; Svedhem, H.; Marty, J. C. "First ever in situ observations of Venus' polar upper atmosphere density using the tracking data of the Venus Express Atmospheric Drag Experiment (VExADE)". *Icarus*, Volume 217, Issue 2, 2011.
- [6] Storch, J. A.. "Aerodynamic Disturbances on Spacecraft in Free-Molecular Flow", Technical report 20030205 194, The Aerospace Corporation, 2002.
- [7] Tolson, R. H.; Patterson, M. T. and Lyons, D. T., "Magellan windmill and termination experiments", *Proceedings of the 10th International Symposium on Flight Dynamics*, 1995.
- [8] Val Serra, S.; Bonnamy, O.; Witasse, O.; Camino, O., "Venus Express Aerobraking", *Proceedings of the 18th IFAC World Congress*, 2011.
- [9] Warnock, J., "A hidden surface algorithm for computer generated halftone pictures", PhD Thesis, University of Utah, 1969.